Received: 25 July 2022 | Revised: 4 October 2022 | Accepted: 11 October 2022

DOI: 10.1111/ffe.13872

ORIGINAL ARTICLE

FFEMS Fatigue & Fracture of Engineering Materials & Structures WILEY

Comparison on mechanical behavior and microstructural features between traditional and AM AISI 316L

Dario Santonocito[1] | **Stanislava Fintová**[2] | **Vittorio Di Cocco**[3] | **Francesco Iacoviello**[3] | **Giacomo Risitano**[1] | **Danilo D'Andrea**[1]

[1]Department of Engineering, Contrada di Dio (S. Agata), University of Messina, Messina, Italy

[2]Institute of Physics of Materials, Czech Academy of Sciences, Brno, Czech Republic

[3]Department of Civil and Mechanical Engineering, University of Cassino and Southern Lazio, Cassino, Italy

Correspondence
Danilo D'Andrea, University of Messina, Department of Engineering, Contrada di Dio (S. Agata), 98166 Messina, Italy.
Email: dandread@unime.it

Funding information
European Union's Horizon 2020 Research and Innovation Program, Grant/Award Number: 857124; Czech Science Foundation, Grant/Award Number: 19-25591Y

Abstract

The aim of the present work is to investigate the difference in mechanical behavior between AISI 316L obtained by the turning process and that obtained by selective laser melting (SLM). To obtain a correlation between mechanical behavior and microstructure, static tensile and fatigue tests were performed, monitoring the energy release of the material adopting, respectively, the static thermographic method (STM) and the Risitano's thermographic method (RTM). Failure analysis was performed using optical and scanning electron microscopy. The corrosion resistance was evaluated by the double-loop electro-potential reactivation (DL-EPR). Worst mechanical properties, both under static and fatigue loading conditions, loss of corrosion resistance, and heat dissipation compared to traditional stainless steel have been found. These findings can be attributed to microstructural defects typical of the SLM printing technology.

KEYWORDS

additive manufacturing, energy methods, mechanical behavior, microstructure characterization

1 | INTRODUCTION

Additive manufacturing (AM) is an increasingly commonly used manufacturing process today. It was initially thought of as a prototyping technique but now becoming a benchmark for manufacturers in many industries. The gain in terms of visibility of AM is due to the possibility of design new devices with complex shapes,[1] customizable, lightweight,[2] and with less waste of material,[3] especially in the aeronautical[4] and bioengineering[5,6] fields, compared to traditional techniques such as electric discharge machining (EDM),[7,8] turning,[9] and milling.[10] Different materials, both polymeric and metallic, can be adopted for AM processing. One of the high-performance steels is the AISI 316L,[11] which is a kind of austenitic steel that nowadays is commonly used in many industrial applications (aerospace,[12] automotive,[13] and biomedical[5,14]), thanks to its good weldability, machinability, and corrosion resistance.[15,16] Many AM techniques have been developed in recent years, such as selective laser melting (SLM),[17,18] electron beam fusion (EBM),[19] and direct energy deposition (DED).[20] However, the AM of metal powders has characteristic defects[21–23] peculiar to the printing method. They can be addressed to the porosity

induced by incorrect fusion of the powders, or the formation of residual stress and large grain growth due to heat transfer and distribution.[24] Production parameters affect the final microstructure of the device, impairing mechanical properties and corrosion resistance.[25,26] Therefore, it is necessary to perform several tests covering both the static and fatigue properties. Yoon et al.[27] have investigated the influence of build directions on the mechanical properties of AISI 316L produced by SLM. Vertical specimens have shown a reduced strength and premature failure compared to the horizontal ones, due to large voids, while have shown better creep resistance. Braun et al.[28] have studied the effect of hybrid additive and subtractive manufacturing on the fatigue strength of AISI 316L, comparing different post-treatment routes with wrought material. They showed that heat treatments and machining significantly increase fatigue strength (respectively, 17% and 87%). Stern et al.[29] have evaluated the influence of the building orientation, as well as the process-induced defects, performing different fatigue tests on AISI 316L. It has been shown that the distribution of the defects and, thus, the fatigue behavior is strongly related to the building direction, leading to a reduction of fatigue life for the tested 90° specimens of more than 90%. Man et al.[30] investigated the cyclic plasticity and the fatigue properties in low cycle fatigue regime of AISI 316L specimens manufactured via SLM. They noticed two distinctive stages of cyclic softening, analyzed in terms of microstructural changes and deformation mechanisms.

To perform a traditional fatigue test campaign, a huge number of tests with high material and time consumption must be performed. Constant amplitude fatigue tests can take more than 1 month to be performed, testing several specimens to obtain the *S–N* curve of the material.[31] With AM, by changing some printing process parameters, different mechanical properties can be achieved[32]; hence, it would require a very large number of specimens and time, leading to high cost for the industry. On the other hand, rapid test procedures based on the energy release of the material have been developed in the last 30 years for traditional engineering materials. The development of the Risitano's thermographic method (RTM)[33] allows the assessment of the fatigue limit of the material and the *S–N* curve.[34] More recently, the static thermographic method (STM) has been proposed to assess the first damage initiation, that is, the first irreversible energetic release, within the material by monitoring the superficial temperature evolution during a static tensile test. A "limit stress" can be identified when a deviation from the linear thermoelastic trend of the temperature signal is noticed. The STM has been applied to several kinds of materials and compared both with conventional constant amplitude fatigue tests and RTM, showing good agreement.[35,36] Santonocito et al. proposed the energy release as a parameter to investigate the fatigue behavior of AM metallic materials.[37]

The aim of this work is the comparison between traditional AISI 316L specimens and AM specimens of the same material. To obtain a correlation between mechanical behavior and microstructure, static tensile and fatigue tests were performed, monitoring the energy release of the material, adopting, respectively, the STM and the RTM. Furthermore, to correlate the mechanical behavior of the material with the microstructural characteristics of the AISI 316L, failure analysis was performed in terms of scanning electron microscopy (SEM).

2 | THEORETICAL BACKGROUND

The first researcher to apply infrared (IR) thermography for the fatigue assessment of materials was Risitano in

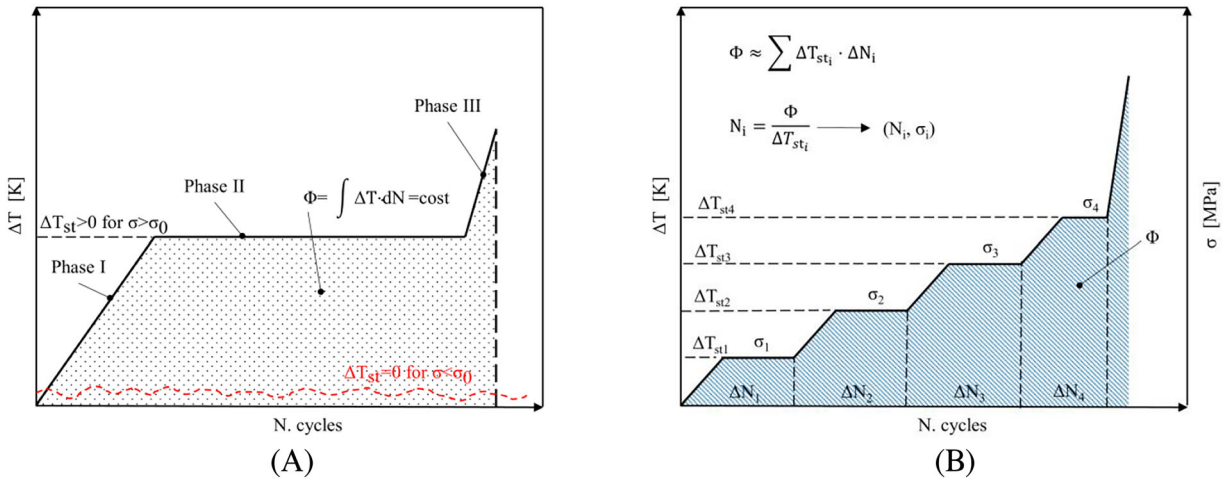

FIGURE 1 Temperature evolution during: (A) constant amplitude and (B) stepwise fatigue tests [Colour figure can be viewed at wileyonlinelibrary.com]

1986.[38] In 2000, La Rosa and Risitano proposed the thermographic method to derive the fatigue life of the material in a very short amount of time.[33] When a material is cyclically stressed above its fatigue limit, it is possible to observe three different phases in the temperature signal (Figure 1A): an initial increment (Phase I), a plateau region (Phase II), and a further increment till the material failure (Phase III). The higher the applied stress, the higher the stabilization temperature of Phase II, but the subtended area of the temperature versus number of cycles curve is constant and equal to an energy parameter Φ. If several stress levels are applied in a stepwise way[34] (Figure 1B), it is possible to obtain the different stabilization temperatures for each stress level. The fatigue limit can be found as the intersection of the temperature versus stress curve with the stress axis (i.e., no temperature increment is noticed above the fatigue limit). The *S–N* curve of the material can be found by exploiting the constancy of the energy parameter (Figure 1B).

Among the rapid fatigue assessment methods, the STM has shown the possibility to obtain rapidly the first damage initiation within the material, that is, the so-called limit stress σ_{lim}. In the last 10 years, several works have shown the relationship between the limit stress and the fatigue limit. Corigliano et al.[35] compared the limit stress of a structural steel with its fatigue limit assessed by RTM and traditional fatigue tests showing good agreement.

The STM is based on the evolution of the temperature trend during a static tensile test. As observed by Risitano and Risitano,[39] during a static tensile test of common engineering materials, the temperature signal exhibits three different phases (Figure 2). The first phase (Phase I) is characterized by an initial approximately linear decrease due to the thermoelastic effect described by the Lord Kelvin's law. All the material's crystals are stressed in a reversible elastic way. In the second phase (Phase II), crystals plasticize and the temperature deviates from the first linear trend until a minimum temperature value is reached. In the last third phase (Phase III), where the plastic deformations are more predominant than the elastic ones, the temperature experiences a very high further increment until material failure (Phase III).

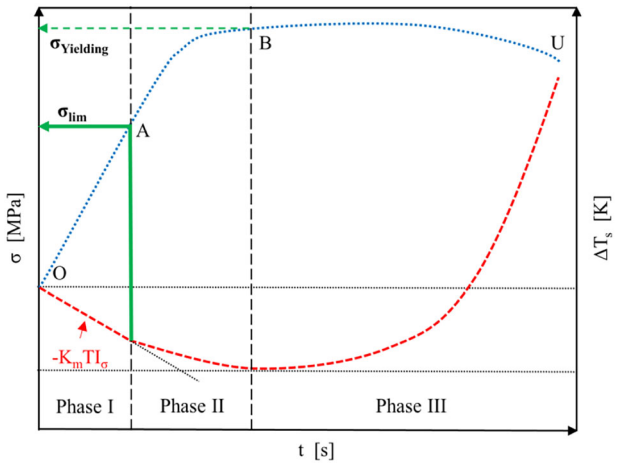

FIGURE 2 Temperature trend during a static tensile test [Colour figure can be viewed at wileyonlinelibrary.com]

Under uniaxial stress state and in adiabatic test conditions, the Lord Kelvin's law can be expressed as Equation (1):

$$\Delta T_s = -K_m T I_\sigma = -\frac{\alpha}{\rho c} T I_\sigma, \tag{1}$$

where the temperature variation ΔT_s depends on K_m, the thermoelastic constant of the material, T, the actual temperature of the specimen, I_σ, the first invariant of the stress tensor. The thermoelastic constant of the material, K_m, is related to the material's physical properties, such as the thermal diffusivity, α, the density, ρ, and the specific heat capacity, c.

For a static tensile test, by monitoring the superficial temperature of the specimen with an IR camera, it is possible to report the stress signal versus the temperature signal. The transition point between Phase I and Phase II can be related to a macroscopic stress level, the limit stress, able to produce within the material microcracks. If that stress level is applied in a cyclic way to the specimen, it will lead to fatigue failure. Clienti et al.[40] identified the limit stress on notched PVC specimens and compared it with the fatigue limit found with RTM at $R = -1$ for the same specimens. The two assessed values were in good agreement. Santonocito,[41] for the first time, applied the STM on 3D-printed PA12 specimens. Constant amplitude fatigue tests were performed at a stress level equal to the limit stress, showing both failure and run-out for the specimens. For a more complete overview of the RTM and STM, the authors remand to previous studies.[33–35,39]

3 | MATERIALS AND METHODS

3.1 | Specimen and material properties

The same specimen's geometry was used for the static tensile and fatigue tests. A first set of specimens was machined by turning from a rolled bar of AISI 316L. This set will be indicated as "Traditional" to distinguish it from the second set, obtained by 3D printing. AM specimens were obtained adopting a SLM printer 3D4Steel® (3D4Mec, Italy). They were printed along the *Z* direction, with a laser power of 230 W and a laser scanning speed of 1400 mm/s (Figure 3A). The height of each layer was

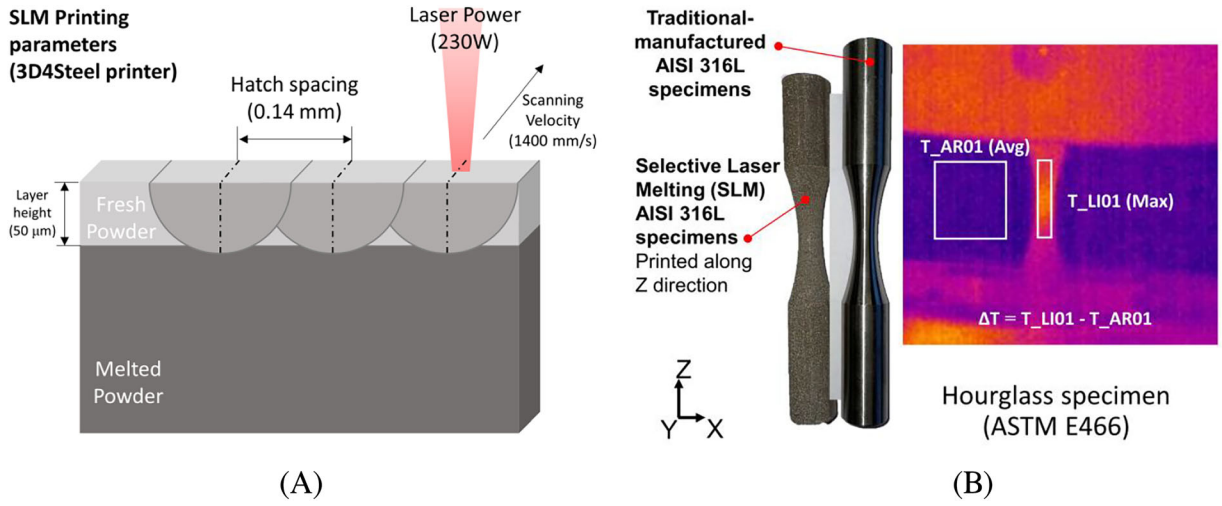

FIGURE 3 (A) SLM printing parameters and (B) AISI 316L specimens and infrared camera test setup [Colour figure can be viewed at wileyonlinelibrary.com]

TABLE 1 AISI 316L composition (in wt%)

AISI 316L	Mn	Cr	Mo	Ni	Cu	Fe
Traditional	1.73	16.68	1.98	10.22	0.37	68.6
AM	1.81	16.99	2.57	12.83	0.037	63.9

50 µm with a hatch spacing of 0.14 mm. The printing process was performed in nitrogen atmosphere with a printing volume of 210 × 210 × 230 mm^3. The loading axis was the same of the rolling/printing direction. The hourglass geometry of the specimens meets the ASTM E466 standard ("Continuous radius between ends", Figure 3B).

The composition of the AISI 316L alloy of the two types of specimens was carried out by means of an X-ray fluorescence (XRF) (SPECTRO, AMETEK, Germany) analysis, as shown in Table 1.

3.2 | Mechanical tests

The AM specimens were tested in the "as-built" conditions. No thermal or superficial treatment was performed. The static tensile tests were performed in a stress control regime, adopting a nominal stress rate of 3 MPa/s to ensure adiabatic conditions during the tensile tests. With this stress rate, the specimen does not have the time to exchange heat with the surrounding environment, resulting in a more evident thermal release.

The stepwise fatigue tests were performed on four specimens adopting two stress ratios ($R = -1$ and $R = 0.1$), with two test frequencies of 10 and 20 Hz and a number of cycles per block ΔN of 10,000 cycles. During all the tests, the temperature trend was monitored with the FLIR A40 IR thermal imaging camera (320 × 240 pixel, thermal sensitivity of 0.08°C a 30°C). For the static tensile test, the acquisition of the thermal images was performed at 50 Hz, while for the fatigue tests, an image every 10 cycles were recorded.

3.3 | Microstructural characterization

An analysis was performed to characterize the microstructure of the stainless steel AISI 316L and to correlate it with the differences in mechanical behavior between the traditional and AM specimens. Microstructure of both the material types was examined using a digital optical microscope (Olympus DSX1000, Tokyo, Japan). Conventional metallographic specimens were prepared in parallel and perpendicular directions to the specimen axis using electrolyte A3 (600 ml methanol, 360 ml, ethylenglykolmonobutylether, 60 ml $HClO_4$) from Struers company. After that, the specimens were dipped into the Beraha II etchand at 28°C for 8 s. To characterize the grain size and potential preferential grain orientation, electron backscatter diffraction (EBSD) analysis was adopted using electrolyte A3 at 40 V for 35 s. The system is a part of Tescan LYRA 3 XMH FEG/SEM scanning electron microscope with a FEG electron source (Tescan, Brno, Czech Republic). A step of 1 µm was used for the EBSD analysis. Grain size was determined based on the misorientation angle of 10°. Potential texture in terms of the grain orientation was determined based on the inverse pole figures (IPFs).

The failure analysis has been carried out using an optical microscope (LEICA Microsystems GmbH,

Germany) and a scanning electron microscope (FEI Quanta 450 FEG, Thermo Fisher Scientific, Waltham, Massachusetts, US). The micro-hardness (FM-300e, Future-Tech Corp, Japan) tests were carried out with a load of 5 N for 15 s. In addition, XRD (ITALSTRUCTURE APD 2000, Cu Kα radiation, 40 kV and 30 mA) tests were performed to compare the crystalline characteristics of the alloys.

3.4 | Corrosion resistance

To evaluate and compare the corrosion resistance of the AM and traditional AISI 316L, double-loop electropotential reactivation (DL-EPR) tests were performed. As a corrosive environment a 0.5 M H_2SO_4 + 0.01 M KSCN aqueous solution was used at laboratory air and temperature. The specimen cleaned in ethanol was used as a working electrode, while a 1 cm^2 area was exposed to the corrosive environment. Before polarization and the corrosion resistance measurement, the open-circuit potential (OCP) was measured for 2 min, then a potential of −450 mV/SCE was kept for 2 min again. The measurement was performed in the potential range from −450 to +200 mV/SCE (sweep rate: 50 mV/min). In order to control results reparability, DL-EPR tests were repeated three times. AM specimens were tested with the as-built surface and the central part (cut ground surface).

4 | RESULTS AND DISCUSSIONS

4.1 | Static tensile test

Static tensile tests have been performed under stress control with a rate of 3 MPa/s. This stress rate is adequate to assure adiabatic test conditions, without dissipation of energy from the specimen to the surrounding environment by convection and conduction. The stress level has been estimated as the ratio between the instantaneous applied force and the middle nominal cross-section area of the specimen. During the tests, the IR camera has been

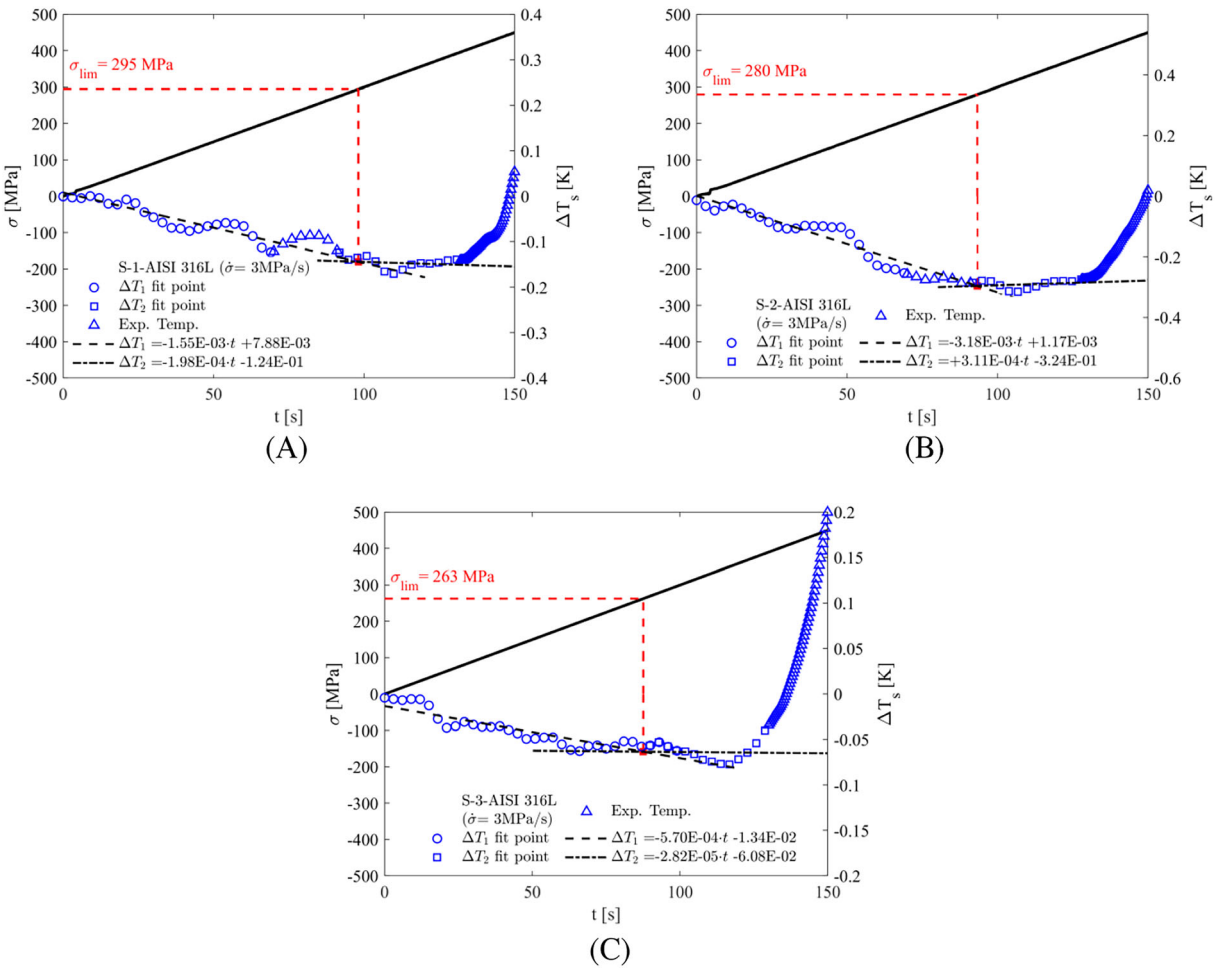

FIGURE 4 Temperature trend during static tensile tests performed on traditional AISI 316L specimens: (A) Specimen Traditional 1, (B) Specimen Traditional 2, and (C) Specimen Traditional 3 [Colour figure can be viewed at wileyonlinelibrary.com]

adopted to monitor the variation of the superficial temperature of the specimen as the difference between the initial temperature value and the instantaneous value. The temperature signal has been filtered with a *rlowess* filter (5% of the whole temperature dataset) to better highlight the temperature signal trend. The stress curve has been plotted versus temperature variation and time to correlate the stress level with the energy release of the material, according to the STM, to assess the limit stress of the material. Three specimens for each material type have been tested and the results have been averaged.

Figure 4 shows the experimental temperature trend of three traditional AISI 316L specimens. In the initial part of the temperature signal, a linear trend can be observed (Phase I, dashed line). Then, the temperature deviates from linearity up to a zero-derivative flex (Phase II, dot-and-dash line). To assess the limit stress, σ_{lim}, it is possible to draw two linear regression lines, respectively, for Phase I (adopting the experimental temperature points of the series "ΔT_1 fit point") and Phase II (adopting the experimental temperature points of the series "ΔT_2 fit point") and determine their equations. The temperature points of the series "Exp. Temperature" have not been adopted to assess the regression lines. By solving the system of the two equations, the coordinates of the intersection point of the two straight lines can be determined. For the traditional AISI 316L, the value of the limit stress determined by the STM is equal to $\sigma_{lim} = 279 \pm 16$ MPa.

The same procedure has been applied to AM AISI 316L specimens (Figure 5) adopting the same stress rate of 3 MPa/s. The AM specimens show both Phase I and Phase II as the traditional counterpart. The minimum temperature decrement is equal to the traditional AISI 316L specimens (about −0.3 K); however, the transition point between Phase I and Phase II is noticed for a lower stress level compared to the traditional ones. For the three AM specimens tested, the average value of the limit stress is equal to $\sigma_{lim} = 191 \pm 17$ MPa.

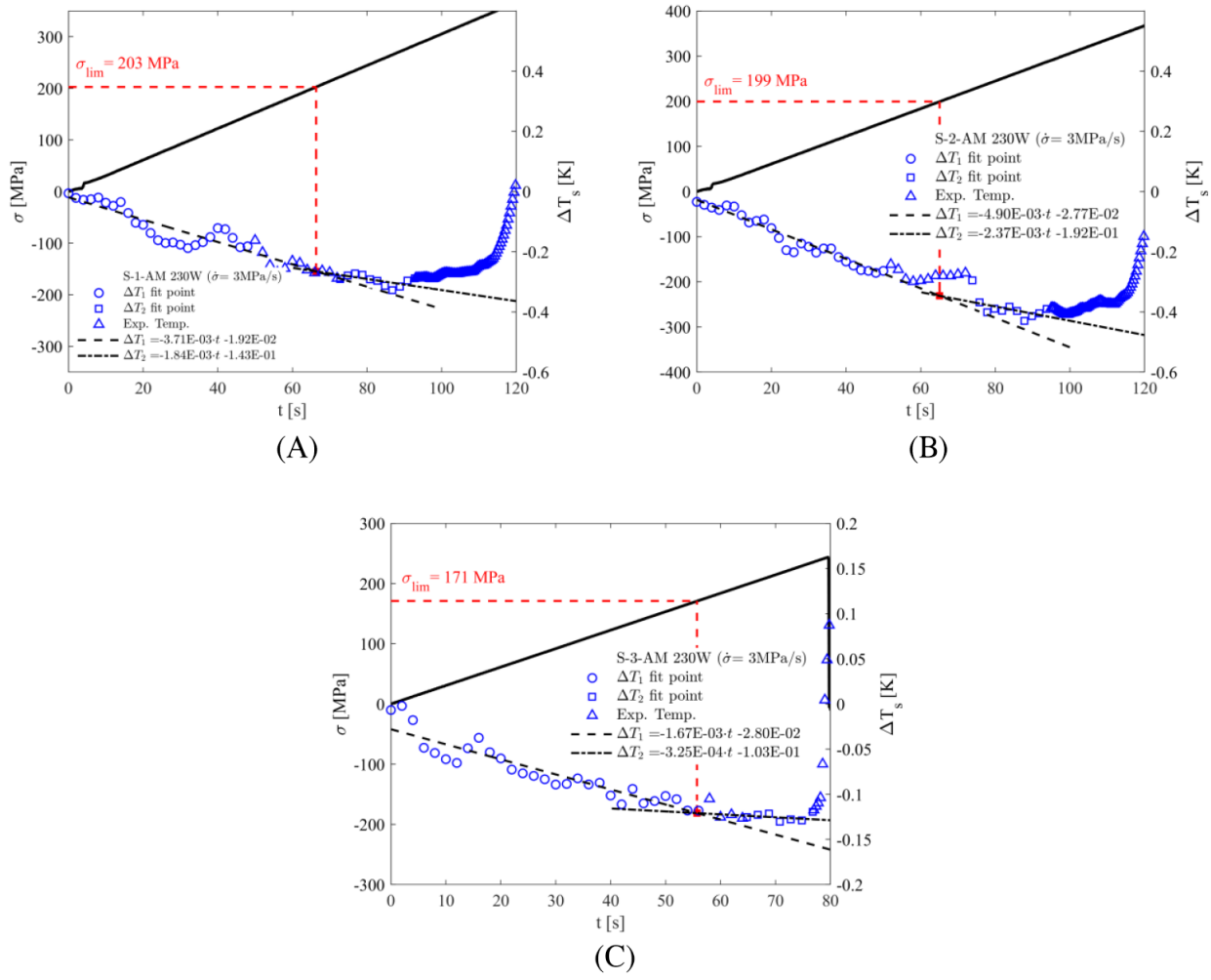

FIGURE 5 Temperature trend during static tensile tests performed on AM AISI 316L specimens: (A) Specimen AM 1, (B) Specimen AM 2, and (C) Specimen AM 3 [Colour figure can be viewed at wileyonlinelibrary.com]

The ultimate tensile strength, σ_U, and the limit stress, σ_{lim}, obtained for each tested specimen have been reported in Table 2. The ultimate tensile strength of the traditional specimens is considerably higher compared to the AM ones (722 MPa for traditional; 329 MPa for AM). On the other hand, the ultimate tensile strength of the AM specimens exhibits a higher scatter (one standard deviation of 11 MPa for traditional; 74 MPa for AM).

According to Risitano and Risitano,[39] the limit stress can be linked to a macroscopic stress level that activates within the material irreversible plastic damage. For the performed tests, it is higher for the traditional material compared to the AM one. While the ultimate tensile strength was 54% higher for the traditional material, only a 20% decrease in the case of limit stress for the AM material has been observed, considering the average values. Since some level of porosity is usually present in the AM materials, such characteristics could be addressed to the microstructure of the material and to the presence of defects.

4.2 | Fatigue test

Stepwise fatigue tests have been performed on traditional specimens adopting stress ratios of $R = -1$ and 0.1, and testing frequencies of 10 and 20 Hz. Two specimens for each combination of stress ratio and frequency have been tested. According to the RTM, the different stabilization temperatures, ΔT_{st}, for each stress level and the energy parameter, Φ, of the specimens have been evaluated.

Figure 6A reports a stepwise fatigue test performed at $R = -1$ and $f = 10$ Hz on a traditional AISI 316L specimen. The stress level has been increased in a stepwise way, and the stabilization temperature has been recorded. For low stress levels (under 260 MPa), the temperature increments are below 5 K. However, as the applied stress level increases, the dissipated energy, directly related to the surface temperature of the specimen, reaches a higher level. For the last stress level (330 MPa), the temperature continues to increment up to the specimen's failure. The same temperature behavior,

TABLE 2 Test results for AISI 316L

Specimen type	No. specimen	σ_U (MPa)	σ_{lim} (MPa)	$\sigma_{U\ ave}$ (MPa)	$\sigma_{lim\ ave}$ (MPa)
AISI 316L traditional	1	715	295	722 ± 11	279 ± 16
	2	716	280		
	3	734	263		
AISI 316L AM (230 W)	1	370	203	329 ± 74	191 ± 17
	2	373	199		
	3	244	171		

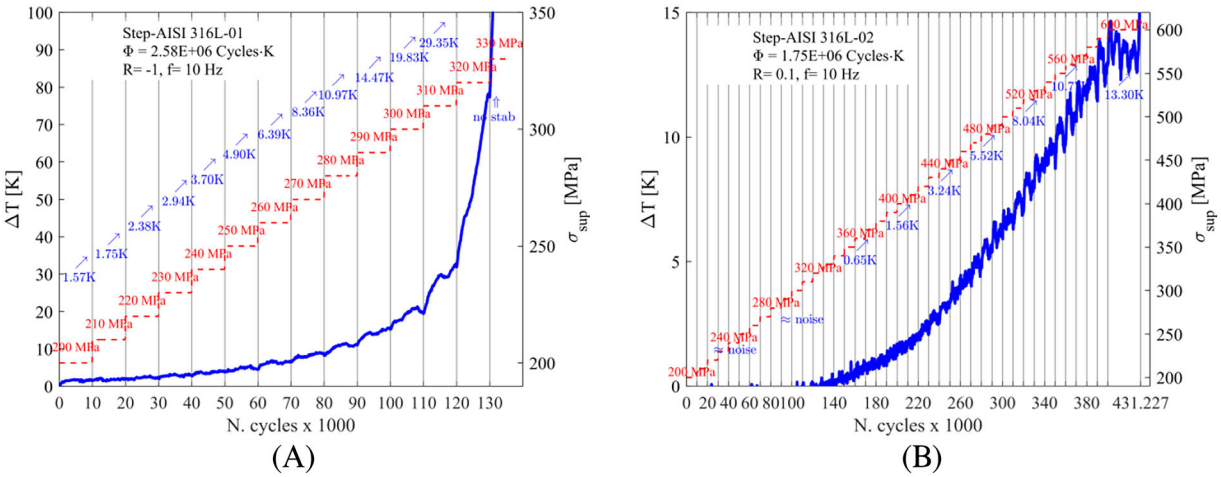

FIGURE 6 Temperature evolution during a stepwise fatigue test of traditional AISI 316L at different stress ratios and frequency of 10 Hz: (A) $R = -1$ and (B) $R = 0.1$ [Colour figure can be viewed at wileyonlinelibrary.com]

but with a noisier signal, can be noticed for a stepwise fatigue test performed at $R = 0.1$, with the same frequency of the previous test. In this case, significative temperature increments are present for a stress level equal to 320 MPa. Temperature increments are lower compared to the ones of the specimens tested at $R = -1$.

To assess the fatigue limit according to RTM, it is possible to plot the different stabilization temperatures versus the applied stress levels (Figure 7). Two straight lines can be defined, one for stress levels below the fatigue limit and the other one for stress levels above the fatigue limit. The intersection of the two straight lines, near the knee region of Figure 7, corresponds to stress levels where fatigue damage begins; hence, it can be related to the fatigue limit of the material.

For traditional AISI 316L tested with stepwise fatigue test, with stress ratio $R = -1$, a value of fatigue limit $\sigma_{0,\ RTM} = 274$ MPa has been found, while a fatigue limit of $\sigma_{0',\ RTM} = 434$ MPa has been found for $R = 0.1$. The energy parameter Φ of the traditional specimens is almost constant for all of the tested specimens. It is equal, respectively, to 1.6×10^6 cycles·K for $R = -1$ and 1.8×10^6 cycles·K for $R = 0.1$.

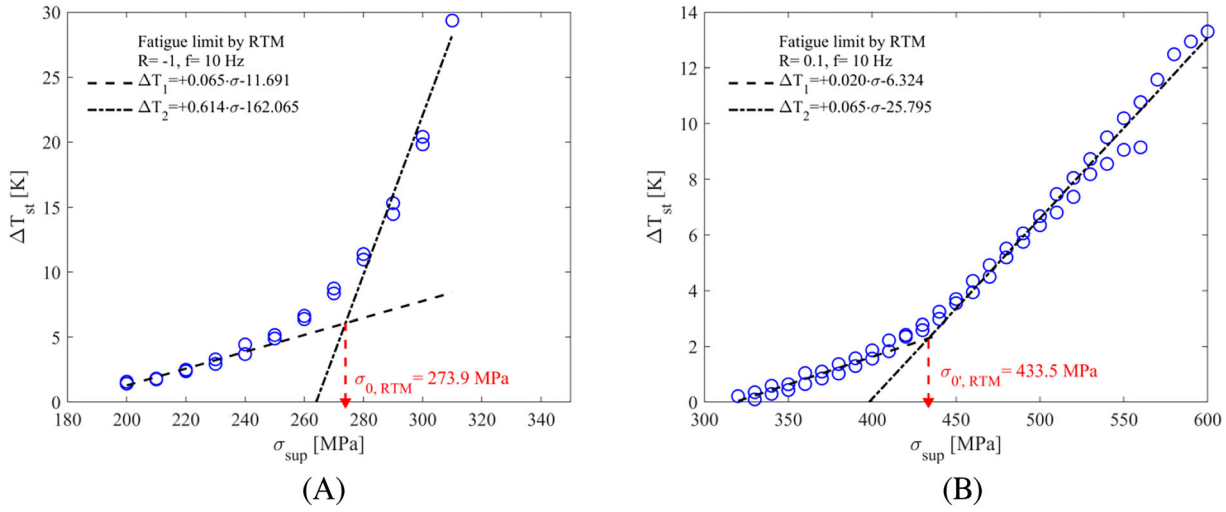

FIGURE 7 Stabilization temperature versus applied stress level for traditional AISI 316L for different stress ratios: (A) $R = -1$ and (B) $R = 0.1$ [Colour figure can be viewed at wileyonlinelibrary.com]

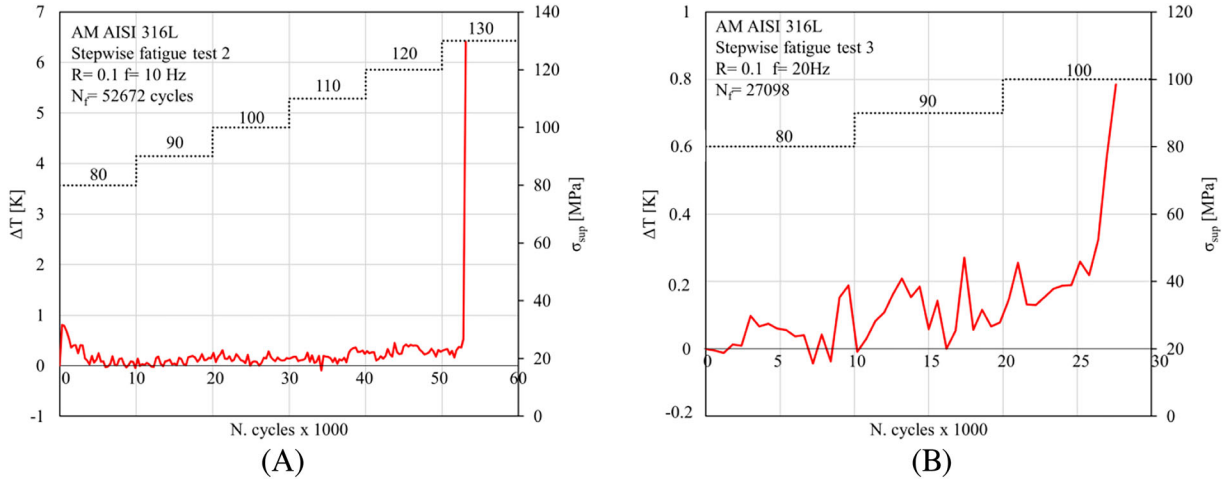

FIGURE 8 Temperature evolution during a stepwise fatigue test for AM AISI 316L at different frequency: (A) 10 and (B) 20 Hz [Colour figure can be viewed at wileyonlinelibrary.com]

The AM specimens have shown a completely different fatigue and energetic behavior compared to the traditional ones. They have been tested in the same way of the traditional specimens, adopting a stress ratio $R = 0.1$ and testing frequencies of 10 and 20 Hz. The tests were performed on two specimens per frequency. However, very premature failure has been recorded, with a very low and noisy temperature increment (Figure 8). The temperature signal shows no increment as the applied stress level is increased. Instead, when the specimen fails, the temperature exhibits a sudden increase considerably smaller compared to the traditional specimens. It has not been possible to estimate the different stabilization temperatures, as well as the energy parameter Φ. No further thermographic elaboration has been possible on such specimens due to the very noisy temperature signal. Such issue can be related to the presence of internal defects that can have an impact on the heat conduction phenomena, as well as on the temperature distribution within the material.

Figure 9 reports the results of the stepwise fatigue tests performed on the AM specimens with other literature data,[42,43] expressed as the maximum applied stress level, σ_{sup}, versus the number of cycles to failure. It can be seen how AM specimens, tested with a stepwise increase of the stress level (black and red full diamonds), show premature and unexpected fatigue failure compared to other AISI 316L AM specimens built along the Z direction (hollow diamonds, as built [AB], machined [M], stress relieved [SR], and no stress relieved [NSR]). Fatigue life of the tested AM specimens cannot be evaluated adopting the RTM due to the noisy temperature signal.

In the same figure, the S–N points for the traditional AISI 316L are reported (black and red full diamonds). They have been obtained according to the RTM exploiting the constancy of the energy parameter. It can be seen how they fall within the area of other AM specimens (hollow square and triangle). However, a constant amplitude (CA) fatigue test campaign must be performed to validate the S–N points obtained by the RTM and the limit stress from the STM.

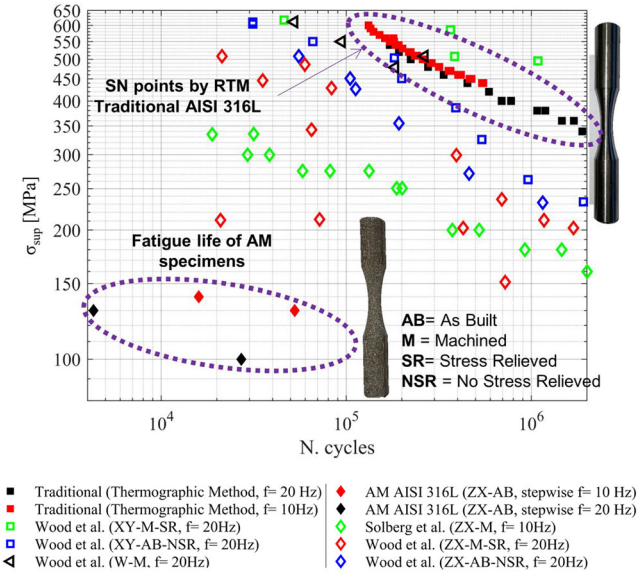

FIGURE 9 Comparison between fatigue data from literature at $R = 0.1$ [Colour figure can be viewed at wileyonlinelibrary.com]

4.3 | XRD and hardness

The XRD spectra obtained for the traditional and AM specimens are shown in Figure 10. The curves clearly

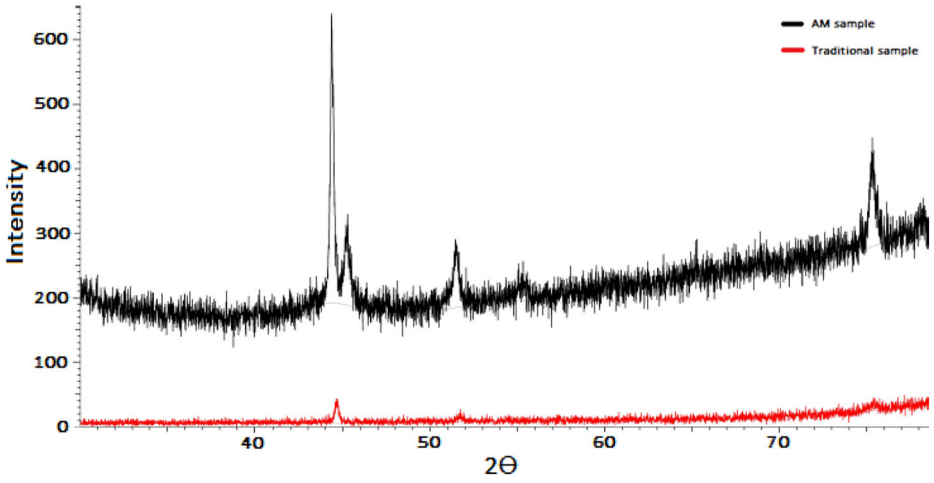

FIGURE 10 XRD comparison between AM and traditional sample [Colour figure can be viewed at wileyonlinelibrary.com]

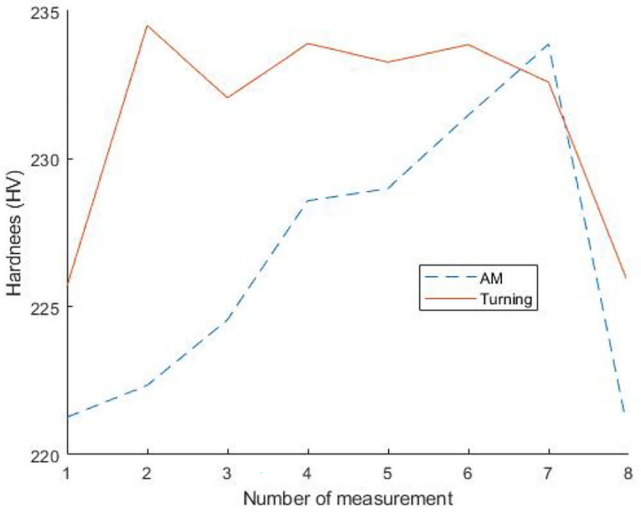

FIGURE 11 Micro-hardness measurement for AM and traditional AISI 316L [Colour figure can be viewed at wileyonlinelibrary.com]

TABLE 3 Average value of micro-hardness for AM and traditional specimens

Specimen type	Micro-hardness (HV0.5)
AISI 316L traditional	231.45 ± 3
AISI 316L AM	226.47 ± 6

show that both the traditional and the AM specimens are characterized by the presence of the FCC austenite phase. In fact, the peaks at 44.5°, 50.5°, and 75° are characteristic of the austenitic phase,[44] while in the case of the AM curve, the first peak is due to the resin and should not be considered. However, as can be seen by comparing XRD spectra, the difference in intensity of the peaks is due to the analyzed area of the sample, which in the case of the AM sample is smaller than the traditional one.

The results of the micro-hardness measurements for the traditional and AM AISI 316L specimens are shown in Figure 11. By analyzing the figure, it is possible to observe that the trend of the Vickers hardness (HV) values for the traditional specimen follow an almost constant trend, while the distribution of hardness values for the AM sample has a greater variability. This behavior is due to the structural inhomogeneity that characterizes the specimen in AM as will be described in the next paragraph. The average hardness value obtained from eight measurements, shown in Table 3, is also higher for the traditional AISI 316L than for the AM one.

4.4 | Microstructure

The typical microstructure of the tested materials is shown in Figure 12. A slight texture can be seen in the case of the traditional material due to the rolling direction (loading direction) while the microstructure consists of polyhedral grains of austenite. Twins are present in the microstructure as a consequence of material processing. Elongated areas of delta ferrite can be seen in Figure 12A, parallel to the rolling direction. The microstructure can be considered homogeneous from the macroscopic point of view, regardless of the specimen orientation versus the loading axis. The microstructure of the AM material is characterized by splats in the direction parallel to the loading axis. As can be seen in Figure 12C,D, grains grew through the splats. The much coarser microstructure is characteristic of the AM material compared to the traditional steel. Locally, some defects (pores/voids) with a size of tenths of micrometers were present in the AM structure.

Grain orientation and grain size were determined based on the EBD analysis of the specimens. The obtained EBSD maps are shown in Figure 13. Analysis of the EBSD maps with Aztec software allows estimation of grain size for individual materials and directions. The average grain size was determined as the equivalent circle diameter considering a 10° misorientation angle as a threshold for the high-angle grain boundary. The average grain size determined for the traditional AISI 316L steel in the direction parallel to the loading axis is 6.97 ± 1.79 μm and in the direction perpendicular to the loading axis is 7.27 ± 2.09 μm. In

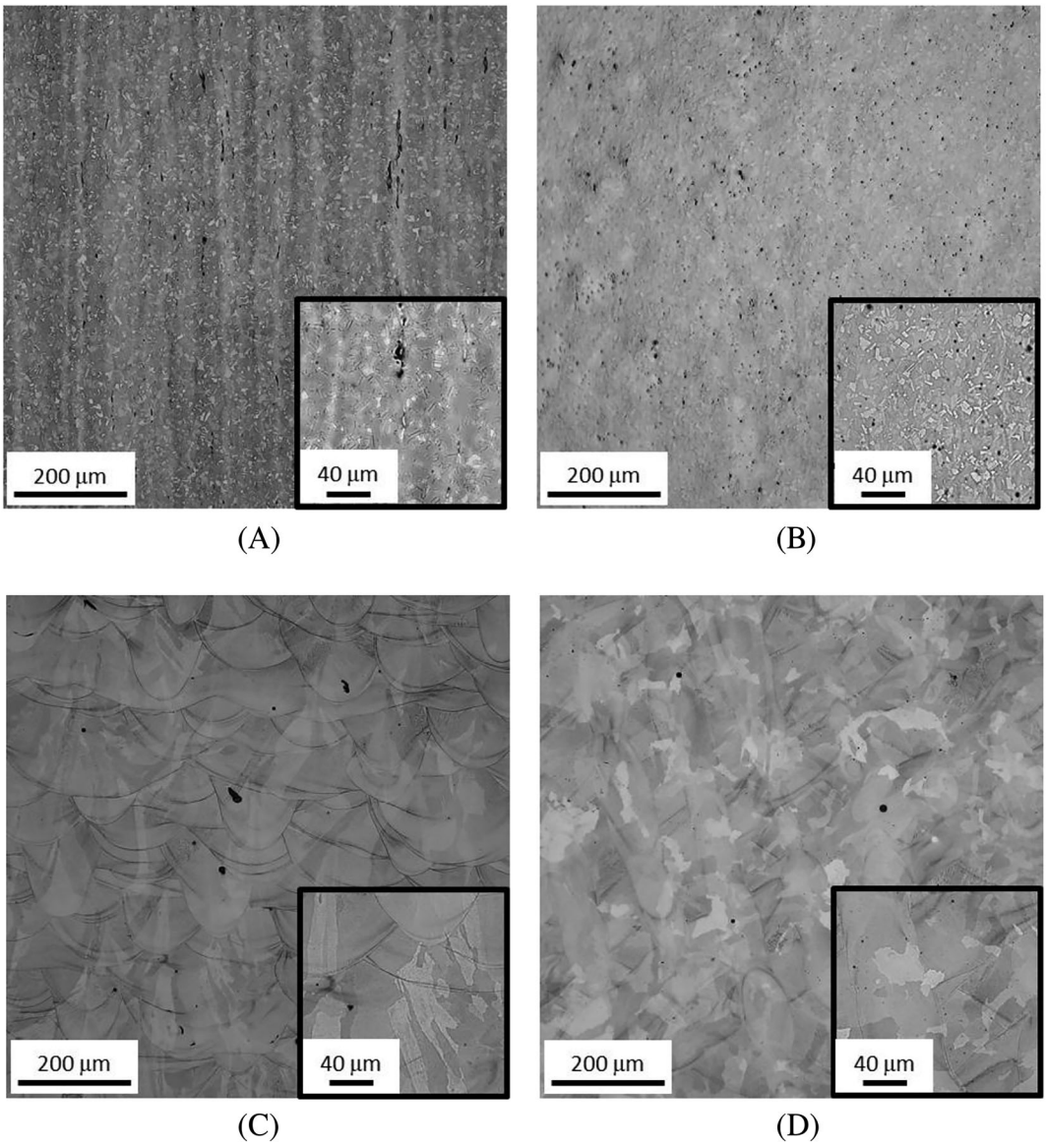

FIGURE 12 A typical microstructure of AISI 316L specimens with inserted details: (A) traditional—parallel to the loading axis, (B) traditional—perpendicular to the loading axis, (C) AM—parallel to the loading axis, and (D) AM—perpendicular to the loading axis

both cases, more than 1300 grains were considered. Present twins were not considered for the average grain size determination. The average grain size determined for the AM AISI 316L steel in the direction parallel to the loading axis is 31.10 ± 24.73 µm and in the direction perpendicular to the loading axis is 27.43 ± 19.00 µm. In both cases, more than 1500 grains were considered. The observed value of standard deviation is quite high due to the specific grain/splats shape. Even though microstructural analysis revealed grains within individual splats growing through several of them, EBSD mapping showed that the grains in one splat exhibited the same or at least similar orientation (misorientation angle below 10°). Taking into account the present IPFs, any preferential grain orientation is observed for both the material states.

The finer microstructure of the traditional material can explain the favorable mechanical properties compared to the AM material.

The fracture surfaces of the specimens obtained by traditional and AM processing after tensile tests show a markedly different morphology (Figure 14). A typical cup-cone fracture surface exhibiting dimple morphology was observed for the traditional material

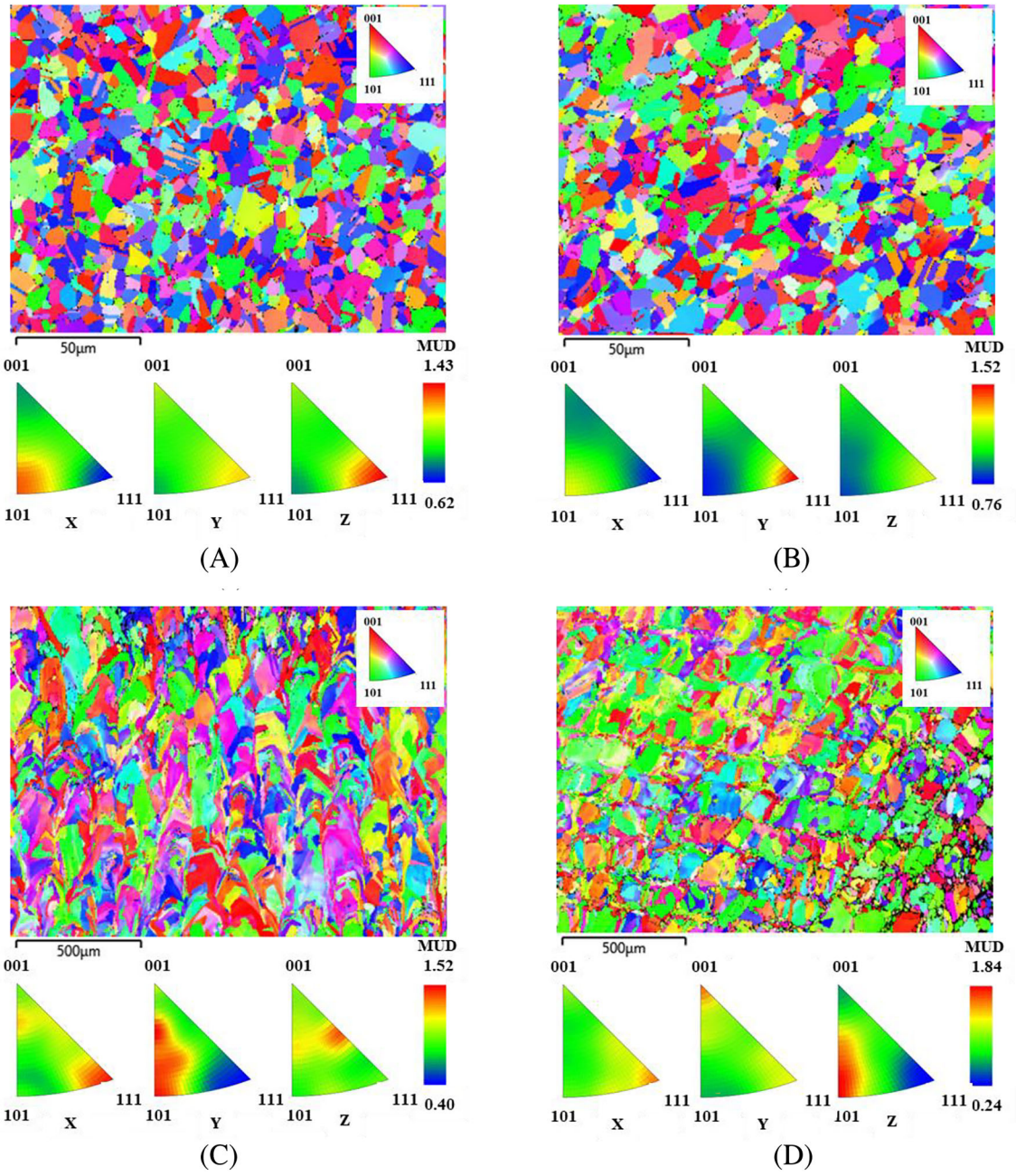

FIGURE 13 EBSD maps of AISI 316L specimens including IPF color key and IPFs showing that the material can be considered as homogeneous without preferential grain orientation: (A) traditional—parallel to the loading axis, (B) traditional—perpendicular to the loading axis, (C) AM—parallel to the loading axis, and (D) AM—perpendicular to the loading axis [Colour figure can be viewed at wileyonlinelibrary.com]

(Figure 14A). On the other hand, lower fracture surface morphology was observed for the AM material (Figure 14B) compared to the traditional one. Partially melted particles, as well as defects, were present on the fracture surface of the AM specimens. This can explain the significant difference in the tensile characteristics presented in Table 2. Since the defects act as the crack initiation sites, the AM specimens reached lower tensile characteristics compared to the traditional material without defects. This is in agreement with other works, showing negative effects of internal defects in AM materials on mechanical properties, such as ductility, toughness, and corrosion resistance.[16] However, also in the case of the AM material, was

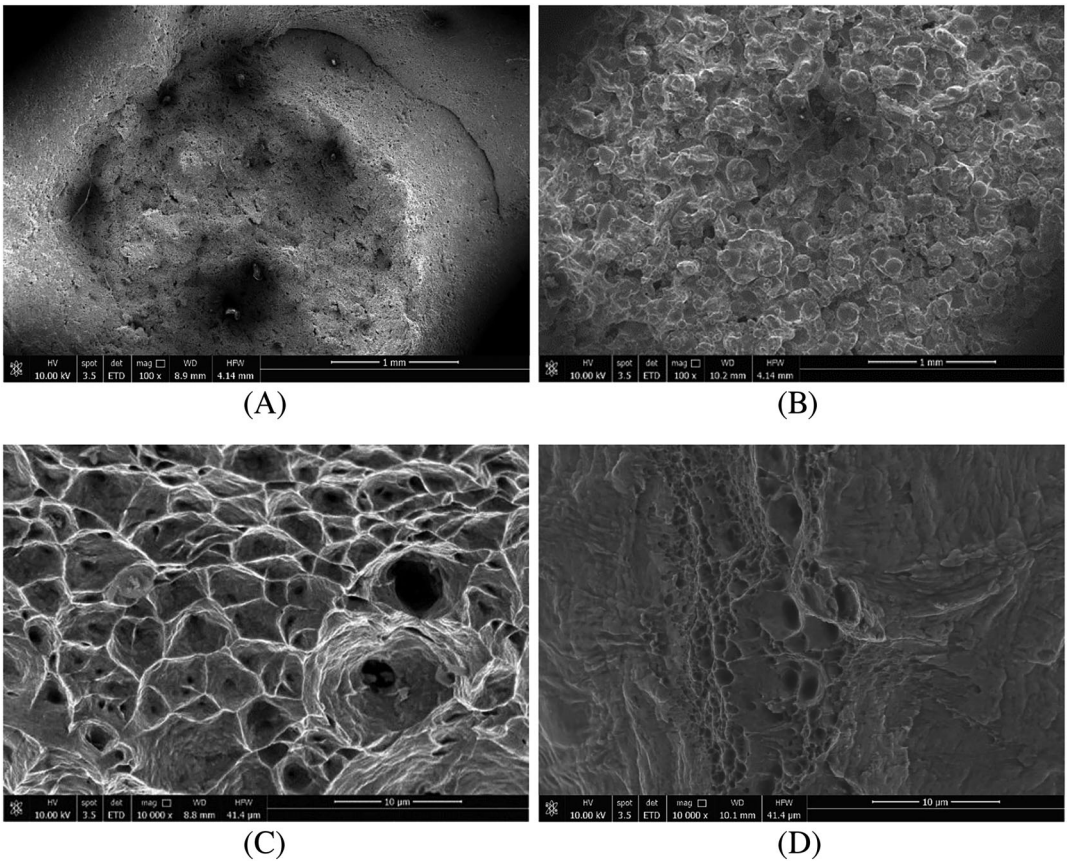

FIGURE 14 Fracture surfaces of AISI 316L specimens after tensile tests: (A) traditional, (B) AM, (C) detail of dimple morphology for traditional material, and (D) detail of fracture morphology for AM material

observed a dimple morphology for the fully compacted areas without internal defects.

The fracture surfaces of specimens broken during fatigue tests were also analyzed in terms of SEM (Figure 15). The traditional specimens exhibited transgranular fracture in the fatigue region while the surface fatigue crack initiation was a characteristic feature. The fracture surface was covered with striations. A dimple morphology was characteristic for the final fracture region.

The surface fatigue crack initiation was characteristic also of the AM specimens. In this case, also the transgranular fracture was observed in the fatigue region; however, striations were not observed in the fatigue region. A dimple morphology was observed in the final fracture region. In the case of AM specimens, internal defects like pores and non-melted powder were observed in some localities. These inhomogeneities can have a detrimental effect on material mechanical properties and can act as the stress concentrators resulting in crack initiation. However, in this study, no fatigue crack initiation on the present defects was observed.

4.5 | Corrosion resistance

Figure 16A shows a comparison between the passivation curve of the traditional specimen respect to the AM one. The measurement was performed on the surface of the specimens.

In the graph, a well-developed passivation peak, characterized by a potential of Flade of about −150 mV/SCE and a current density of about 4×10^{-3} mA/cm^2, is shown. This is a traditional behavior of a non-sensitized AISI 316L and the turning operation does not modify the corrosion resistance of the investigated stainless steel, because no reactivation peaks are present in the double loop. Instead, the specimen obtained by AM (red curve in Figure 16A) presents a different corrosion behavior compared to

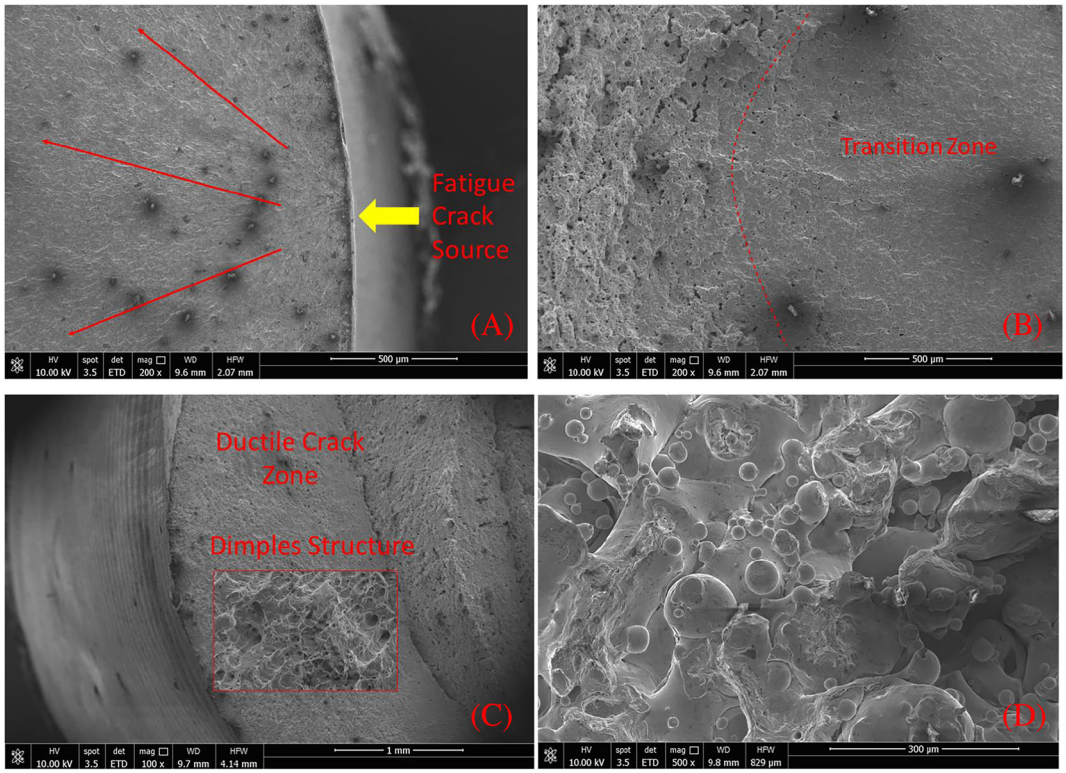

FIGURE 15 SEM images of traditional and AM specimens fatigue fracture surface: (A) traditional—surface fatigue crack initiation marked with a yellow arrow and crack growth direction marked with red arrows, (B) traditional—transition zone, (C) traditional—ductile fracture zone, and (D) AM—unmelted powders particles on fatigue surface [Colour figure can be viewed at wileyonlinelibrary.com]

the traditional one. Two different peaks are present in the direct loop:

- The first one is characterized by a potential of about −120 mV/SCE and current density of about 1.90×10^{-3} mA/cm^2.
- The second one at −40 mV/SCE and 8×10^{-4} mA/cm^2.

The values of the potentials at peaks are positive and greater than the free one. It means that in any investigated conditions the corroding occurs, that is, there are two different phases characterized by different Flade potential, but none is able to generate a passivation layer. Indeed, in the inverse loop the current density never achieves the zero values for potential down to the free one. The observed behavior can be associated to the surface roughness of the as-built surface where the really exposed area can be much higher than 1 cm^2 and the surface morphology can obstruct creation of compact layer of corrosion products protecting material against following corrosion.

Considering the surface of inner (central) part of the specimen obtained cutting the AM specimen (Figure 16B), a single passivation peak is present on the polarization curve and the traditional AISI 316L (Figure 16A), but the Flade potential is greater than the one presented in Figure 16A. It means that the internal part of the components manufactured by additive technique generates a material that requires a different potential to passivate it. Furthermore, a lower reactivation peak is present in the inverse loop, but the value seems to be negligible, mainly if compared to the values recorded on the external part of the additively manufactured specimen. The differences in potentials observed for the AM specimen presented in Figure 16A,B could be due to the printing parameters and present defects. Since a shell was printed to cover the specimen, the structure can be influenced, and preferential grain orientations could be present. In addition, the as-built surface exhibits much higher real surface area exposed to the corrosive medium. Due to the surface roughness of the as-built surface, also the created corrosion products or potentially created surface layer of corrosion products cannot be compact and prove a protection against following corrosion process.

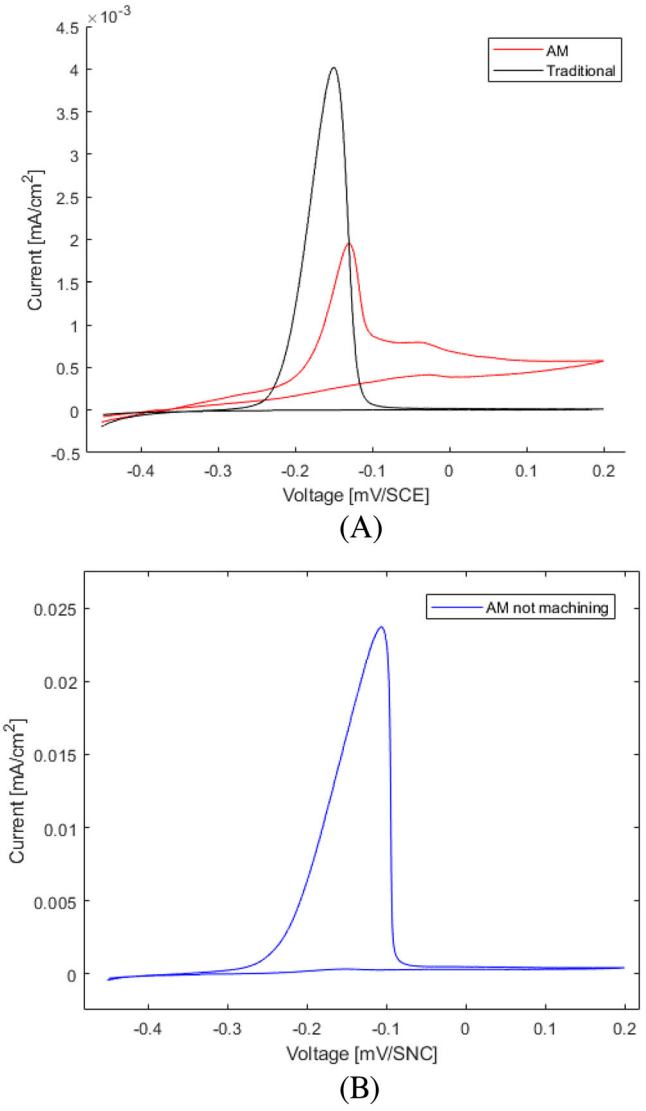

FIGURE 16 Polarization curves: (A) comparison between AM and traditional AISI 316L corrosion behavior and (B) polarization curve of inner part of AM specimen [Colour figure can be viewed at wileyonlinelibrary.com]

5 | CONCLUSION

In this work, static and stepwise fatigue tests were performed on traditional and AM specimens of AISI 316L. IR thermography was adopted to evaluate the temperature trend during static tensile tests, applying the STM, and stepwise fatigue tests, applying the RTM. Chemical and microstructure analyses were performed to evaluate the corrosion resistance and to correlate the mechanical behavior with the microstructure of the 3D-printed specimens.

The most important results are the following:

- AM specimens exhibit lower mechanical properties, both under static and fatigue loading than traditional material, mostly due to their microstructure. The presence of numerous defects, such as unfused powders and voids/pores, impairs the mechanical properties of the AM AISI 316L. Furthermore, the difference in mechanical behavior is due to the grain size, which is greater in AM specimens.
- AM specimens lose the typical corrosion resistance of stainless steel.
- The hardness value of the AM sample is lower and more variable than the traditional one, due to subsurface defects that affect the measurement.
- The application of the RTM and STM methods in AM specimens is more difficult than with traditional material. The AM stainless steel, probably due to the crystalline structure given by the printing process, does not have a good thermal conductivity; hence, there is no appreciable increase in temperature as in the case of traditional material.

To determine the effect of the printing parameters on the material microstructure and to evaluate the effect of heat treatments on the mechanical properties of the samples, several static and fatigue tests must be performed. Furthermore, it will be interesting to investigate the possible causes of the difference in thermal behavior between the printed material and the traditional one.

ACKNOWLEDGMENTS

This research was partially funded by research grant from the European Union's Horizon 2020 Research and Innovation Program (H2020-WIDESPREAD-2018) under Grant Agreement No. 857124, SIRAMM. The authors are grateful for financial support of the Czech Science Foundation by the project 19-25591Y.

DATA AVAILABILITY STATEMENT

The data that support the findings of this study are available from the corresponding author upon reasonable request.

NOMENCLATURE

AM	additive manufacturing
c	specific heat capacity of the material (J/kg. K)
CA	constant amplitude
DED	direct energy deposition
DL-EPR	double-loop electropotential reactivation
EBM	electron beam melting
EBSD	electron backscatter diffraction
EDM	electric discharge machining
f	test frequency (Hz)
FCC	face-centered cubic
IR	infrared
I_σ	first invariant of the stress tensor (MPa)

K_m	thermoelastic coefficient (MPa^{-1})
N, N_f	number of cycles, number of cycles to failure
R	stress ratio
RTM	Risitano's thermographic method
SLM	selective laser melting
STM	static thermographic method
t	test time (s)
T, T_i	instantaneous value of temperature (K)
T_0	initial value of temperature estimated at time zero (K)
XRD	X-ray diffraction
XRF	X-ray fluorescence
α	thermal diffusivity of the material (m^2/s)
ΔN_i	number of cycle block length
ΔT	absolute surface temperature variation during a fatigue test (K)
ΔT_s	absolute surface temperature variation during a static tensile test (K)
ΔT_{st}	stabilization temperature for fatigue tests (K)
ΔT_1	estimated value of temperature for the first set of temperature data (K)
ΔT_2	estimated value of temperature for the second set of temperature data (K)
Φ	energy parameter (cycles·K)
Φ_{ave}	average value of the energy parameter (cycles·K)
ρ	density of the material (kg/m^3)
σ	stress level (MPa)
σ_{lim}	limit stress according to STM (MPa)
$\sigma_{yielding}$	yield stress (MPa)
σ_{Sup}	maximum applied stress (MPa)
$\sigma_{0,\ RTM}$	fatigue limit ($R = -1$) estimated with the RTM (MPa)
$\sigma_{0',\ RTM}$	fatigue limit ($R = 0.1$) estimated with the RTM (MPa)
$\dot{\sigma}$	stress rate (MPa/min)

ORCID

Stanislava Fintová https://orcid.org/0000-0002-2460-2933
Francesco Iacoviello https://orcid.org/0000-0002-9382-6092
Giacomo Risitano https://orcid.org/0000-0002-0506-8720
Danilo D'Andrea https://orcid.org/0000-0002-9809-8434

REFERENCES

1. Epasto G, Palomba G, Andrea DD, et al. Experimental investigation of rhombic dodecahedron micro-lattice structures manufactured by Electron Beam Melting. *Mater Today: Proc*. 2019; 7:578-585.
2. Plocher J, Panesar A. Review on design and structural optimisation in additive manufacturing: towards next-generation lightweight structures. *Mater Des*. 2019;183:108164.
3. Yang L, Hsu K, Baughman B, et al. *Additive Manufacturing of Metals: The Technology, Materials, Design and Production*. Springer; 2017.
4. Pradeep PI, Kumar VA, Sriranganath A, et al. Characterization and qualification of LPBF additively manufactured AISI-316L stainless steel brackets for aerospace application. *Trans Indian Natl Acad Eng*. 2020;5(3):603-616.
5. Tilton M, Lewis GS, Bok Wee H, Armstrong A, Hast MW, Manogharan G. Additive manufacturing of fracture fixation implants: design, material characterization, biomechanical modeling and experimentation. *Addit Manuf*. 2020;33:101137.
6. Chen RK, Jin Y, Wensman J, Shih A. Additive manufacturing of custom orthoses and prostheses—a review. *Addit Manuf*. 2016;12:77-89.
7. Jain S, Parashar V. Critical review on the impact of EDM process on biomedical materials. *Mater Manuf Process*. 2021; 36(15):1701-1724.
8. D'Andrea D, Pistone A, Risitano G, Santonocito D, Scappaticci L, Alberti F. Tribological characterization of a hip prosthesis in Si3N4-TiN ceramic composite made with Electrical Discharge Machining (EDM). *Procedia Struct Integr*. 2021; 33:469-481.
9. Khanna N, Shah P, de Lacalle LNL, Rodríguez A, Pereira O. In pursuit of sustainable cutting fluid strategy for machining Ti-6Al-4V using life cycle analysis. *Sustain Mater Technol*. 2021; 29:e00301.
10. Gómez-Escudero G, Jimeno Beitia A, de Pissón M, Caruncho G, et al. A reliable clean process for five-axis milling of knee prostheses. *Int J Adv Manuf Technol*. 2021;115(5–6): 1605-1620.
11. D'Andrea D, Guglielmino E, Risitano G, Santonocito D. Rapid determination of the fatigue behavior at different stress ratios of steels by measuring the energy release. In: *European Workshop on Structural Health Monitoring*. Springer; 2023: 589-599.
12. Pirrone SRM, Agabiti C, Pagan AS, Herdrich G. A fast thermal 1D model to study aerospace material response behaviors in uncontrolled atmospheric entries. *Materials (Basel)*. 2022;15(4): 1505.
13. Mohammed HG, Ginta TL, Mustapha M. The investigation of microstructure and mechanical properties of resistance spot welded AISI 316L austenitic stainless steel. *Mater Today Proc*. 2020;46:1640-1644.
14. Brończyk A, Kowalewski P, Samoraj M. Tribocorrosion behaviour of Ti6Al4V and AISI 316L in simulated normal and inflammatory conditions. *Wear*. 2019;434:202966.
15. Godec M, Donik KA, Podgornik B, Skobir Balantič DA. Effect of post-treated low-temperature plasma nitriding on the wear and corrosion resistance of 316L stainless steel manufactured by laser powder-bed fusion. *Addit Manuf*. 2020;32:101000.
16. Kurgan N, Varol R. Mechanical properties of P/M 316L stainless steel materials. *Powder Technol*. 2010;201(3):242-247.
17. Simson T, Emmel A, Dwars A, Böhm J. Residual stress measurements on AISI 316L samples manufactured by selective laser melting. *Addit Manuf*. 2017;17:183-189.

18. D'Andrea D, Risitano G, Guglielmino E, Piperopoulos E, Santonocito D. Correlation between mechanical behaviour and microstructural features of AISI 316L produced by SLM. *Procedia Struct Integr*. 2022;41:199-207.
19. Epasto G, Palomba G, D'Andrea D, Guglielmino E, Di Bella S, Traina F. Ti-6Al-4V ELI microlattice structures manufactured by electron beam melting: effect of unit cell dimensions and morphology on mechanical behaviour. *Mater Sci Eng A*. 2019; 753:31-41.
20. Saboori A, Aversa A, Bosio F, et al. An investigation on the effect of powder recycling on the microstructure and mechanical properties of AISI 316L produced by Directed Energy Deposition. *Mater Sci Eng A*. 2019;766:138360.
21. Saboori A, Toushekhah M, Aversa A, et al. Critical features in the microstructural analysis of AISI 316L produced by metal additive manufacturing. *Metallogr Microstruct Anal*. 2020;9(1): 92-96.
22. D'Accardi E, Altenburg S, Maierhofer C, Palumbo D, Galietti U. Detection of typical metal additive manufacturing defects by the application of thermographic techniques. *Proceedings*. 2019;27(1):24.
23. Kotzem D, Kleszczynski S, Stern F, et al. Impact of single structural voids on fatigue properties of AISI 316L manufactured by laser powder bed fusion. *Int J Fatigue*. 2021;148: 106207.
24. Afkhami S, Dabiri M, Alavi SH, Björk T, Salminen A. Fatigue characteristics of steels manufactured by selective laser melting. *Int J Fatigue*. 2019;122:72-83.
25. Du Plessis A, Yadroitsava I, Yadroitsev I. Effects of defects on mechanical properties in metal additive manufacturing: a review focusing on X-ray tomography insights. *Mater Des*. 2020;187:108385.
26. Malekipour E, El-Mounayri H. Common defects and contributing parameters in powder bed fusion AM process and their classification for online monitoring and control: a review. *Int J Adv Manuf Technol*. 2018;95(1–4):527-550.
27. Yoon KB, Dao VH, Yu JM. Effects of build direction on tensile and creep properties of 316L stainless steel produced by selective laser melting. *Fatigue Fract Eng Mater Struct*. 2020;43(11): 2623-2636.
28. Braun M, Mayer E, Kryukov I, et al. Fatigue strength of PBF-LB/M and wrought 316L stainless steel: effect of post-treatment and cyclic mean stress. *Fatigue Fract Eng Mater Struct*. 2021; 44(11):3077-3093.
29. Stern F, Kleinhorst J, Tenkamp J, Walther F. Investigation of the anisotropic cyclic damage behavior of selective laser melted AISI 316L stainless steel. *Fatigue Fract Eng Mater Struct*. 2019; 42(11):2422-2430.
30. Man J, Šulák I, Chlupová A, Douša L, Polák J. Cyclic plasticity and LCF behavior of AISI 316L austenitic stainless steel manufactured by selective laser melting (SLM). In: *LCF9 Ninth International Conference on Low Cycle Fatigue*; 2022. DVM e.V.
31. Rigon D, Meneghetti G. Engineering estimation of the fatigue limit of wrought and defective additively manufactured metals for different load ratios. *Int J Fatigue*. 2022;154: 106530.
32. Alfieri V, Giannella V, Caiazzo F, Sepe R. Influence of position and building orientation on the static properties of LPBF specimens in 17-4 PH stainless steel. *Forces Mech*. 2022;8:100108.
33. La Rosa G, Risitano A. Thermographic methodology for rapid determination of the fatigue limit of materials and mechanical components. *Int J Fatigue*. 2000;22(1):65-73.
34. Fargione G, Geraci A, La Rosa G, Risitano A. Rapid determination of the fatigue curve by the thermographic method. *Int J Fatigue*. 2002;24(1):11-19.
35. Corigliano P, Cucinotta F, Guglielmino E, Risitano G, Santonocito D. Fatigue assessment of a marine structural steel and comparison with Thermographic Method and Static Thermographic Method. *Fatigue Fract Eng Mater Struct*. 2020;43(4): 734-743.
36. Ricotta M, Meneghetti G, Atzori B, Risitano G, Risitano A. Comparison of experimental thermal methods for the fatigue limit evaluation of a stainless steel. *Metals (Basel)*. 2019; 9(6):677.
37. Santonocito D, Gatto A, Risitano G. Energy release as a parameter for fatigue design of additive manufactured metals. *Mater Des Process Commun*. 2021;1-7.
38. Curti G, La Rosa G, Orlando M, Risitano A. Analisi tramite infrarosso termico della temperatura limite in prove di fatica. *Proc XIV Convegno Naz AIAS*. 1986;211-220.
39. Risitano A, Risitano G. Determining fatigue limits with thermal analysis of static traction tests. *Fatigue Fract Eng Mater Struct*. 2013;36(7):631-639.
40. Clienti C, Fargione G, La Rosa G, Risitano A, Risitano G. A first approach to the analysis of fatigue parameters by thermal variations in static tests on plastics. *Eng Fract Mech*. 2010; 77(11):2158-2167.
41. Santonocito D. Evaluation of fatigue properties of 3D-printed Polyamide-12 by means of energy approach during tensile tests. *Procedia Struct Integr*. 2020;25:355-363.
42. Solberg K, Guan S, Razavi SMJ, Welo T, Chan KC, Berto F. Fatigue of additively manufactured 316L stainless steel: the influence of porosity and surface roughness. *Fatigue Fract Eng Mater Struct*. 2019;42(9):2043-2052.
43. Wood P, Libura T, Kowalewski ZL, Williams G, Serjouei A. Influences of horizontal and vertical build orientations and post-fabrication processes on the fatigue behavior of stainless steel 316l produced by selective laser melting. *Materials (Basel)*. 2019;12(24):4203.
44. Dadfar M, Fathi MH, Karimzadeh F, Dadfar MR, Saatchi A. Effect of TIG welding on corrosion behavior of 316L stainless steel. *Mater Lett*. 2007;61(11–12):2343-2346.

How to cite this article: Santonocito D, Fintová S, Di Cocco V, Iacoviello F, Risitano G, D'Andrea D. Comparison on mechanical behavior and microstructural features between traditional and AM AISI 316L. *Fatigue Fract Eng Mater Struct*. 2023;46(2):379-395. doi:10.1111/ffe.13872